pH-Responsive Assembly of Gold Nanoparticles and "Spatiotemporally Concerted" Drug Release for Synergistic Cancer Therapy

Jutaek Nam,[†,▲] Wan-Geun La,[‡,▲] Sekyu Hwang,[†] Yeong Su Ha,[§] Nokyoung Park,[⊥] Nayoun Won,[†] Sungwook Jung,[∥] Suk Ho Bhang,[‡] Yoon-Ji Ma,[‡] Yong-Min Cho,[‡] Min Jin,[‡] Jin Han,[‡] Jung-Youn Shin,[‡] Eun Kyung Wang,[§] Sang Geol Kim,[¶] So-Hye Cho,[#] Jeongsoo Yoo,[§] Byung-Soo Kim,[‡,△,*] and Sungjee Kim[†,∥,*]

[†]Department of Chemistry, Pohang University of Science & Technology, San 31, Hyojadong, Namgu, Pohang 790-784, South Korea, [‡]School of Chemical and Biological Engineering, Seoul National University, San 56-1, Sillim-dong, Gwanak-gu, Seoul 151-742, South Korea, [§]Department of Molecular Medicine, School of Medicine, Kyungpook National University, Dongin-dong, Joong-gu, Daegu 700-422, South Korea, [⊥]Frontier Research Laboratory, Samsung Advanced Institute of Technology, Samsung Electronics, Yongin, Kyunggi-do 446-712, South Korea, [∥]School of Interdisciplinary Bioscience and Bioengineering, Pohang University of Science & Technology, San 31, Hyojadong, Namgu, Pohang 790-784, South Korea, [¶]Department of Surgery, School of Medicine, Kyungpook National University, Dongin-dong, Joong-gu, Daegu 700-422, South Korea, [#]Nano-Materials Center, Korea Institute of Science and Technology, P.O. Box 131, Cheongryang, Seoul 130-650, South Korea, and [△]Bio-MAX Institute, Institute of Chemical Processes, Engineering Research Institute, Seoul National University, San 56-1, Sillim-dong, Gwanak-gu, Seoul 151-742, South Korea. [▲]These authors contributed equally.

ABSTRACT

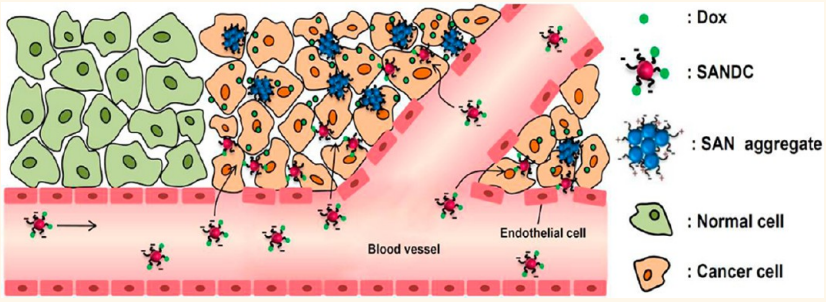

A challenge in using plasmonic nanostructure–drug conjugates for thermo–chemo combination cancer therapy lies in the huge size discrepancy; the size difference can critically differentiate their biodistributions and hamper the synergistic effect. Properly tuning the plasmonic wavelength for photothermal therapy typically results in the nanostructure size reaching ~100 nm. We report a new combination cancer therapy platform that consists of relatively small 10 nm pH-responsive spherical gold nanoparticles and conjugated doxorubicins. They are designed to form aggregates in mild acidic environment such as in a tumor. The aggregates serve as a photothermal agent that can selectively exploit external light by their collective plasmon modes. Simultaneously, the conjugated doxorubicins are released. The spatiotemporal concertion is confirmed at the subcellular, cellular, and organ levels. Both agents colocalize in the cell nuclei. The conjugates accumulate in cancer cells by the rapid phagocytic actions and effective blockage of exocytosis by the increased aggregate size. They also effectively accumulate in tumors up to 17 times over the control because of the enhanced permeation and retention. The conjugates exhibit a synergistic effect enhanced by nearly an order of magnitude in cellular level. The synergistic effect is demonstrated by the remarkable reductions in both the therapeutically effective drug dosage and the photothermal laser threshold. Using an animal model, effective tumor growth suppression is demonstrated. The conjugates induce apoptosis to tumors without any noticeable damage to other organs. The synergistic effect *in vivo* is confirmed by qRT-PCR analysis over the thermal stress and drug-induced growth arrest.

KEYWORDS: gold nanoparticle · pH-responsive · drug delivery · photothermal therapy · synergistic effect · tumor targeting

Combination therapy—the simultaneous use of two or more agents as a "one–two punch"—can be synergistically effective for cancer treatments. For example, the combination of hyperthermia and chemotherapy often results in synergistic interactions between the two modalities, showing enhanced therapeutic efficacy over the two independent treatments.[1−4] Gold nanostructures can generate site-selective local heat shock, and they have great potential as an engineerable platform for thermo–chemo combination cancer therapy. Many research groups have demonstrated the potential of gold nanostructures as a photothermal therapeutic agent by exploiting their

* Address correspondence to byungskim@snu.ac.kr, sungjee@postech.ac.kr.

Received for review January 15, 2013 and accepted March 26, 2013.

Published online March 26, 2013
10.1021/nn400223a

strong absorption and efficient heat conversion.[5−11] In a few cases, they were also co-applied with chemo agents, and these combinations have demonstrated enhanced cytotoxicity toward cancer cells.[12−17] However, gold nanostructures have not been fully exploited for combination therapy. The administration method of the thermo and chemo agents relies primarily on physical mixtures or loosely bound conjugates, which typically rely on electrostatic interactions. As a result, the actions of the thermo and chemo modalities cannot be well-controlled, which prevented them from achieving their maximal synergistic effect. The challenge in using gold nanostructures as an engineerable platform for thermo−chemo combination therapy lies in the huge discrepancy between the sizes of the thermo and chemo agents. The gold nanostructures need to absorb far-red or near-infrared (NIR) light for the photothermal effect to reach deep tissues. Properly tuning the plasmonic wavelength for the far-red or NIR region typically demands large nanostructures such as nanorods, nanoshells, and nanocages of which hydrodynamic sizes typically reach ~100 nm.[5−8,10,11] Most molecule-based chemo agents are far smaller than gold nanostructures. This size difference inherently limits the concertion of the thermo and chemo agents because the size of the agents critically determines their entry to cells and their distribution in confined cellular compartments. Recently, we reported a simple, spherical, 10 nm "smart" Au nanoparticle (abbreviated as SAN) for effective photothermal therapy.[9] The SAN surface was engineered to induce rapid and conditional aggregation in a mildly acidic environment, which shifts the absorption to far-red and NIR by creating the collective plasmon modes. SANs can be advantageous because their small size allows efficient internalization into cancerous cells.[18] In addition, this kind of aggregation-based strategy can utilize small Au NPs that can potentially mitigate side effects by facilitated excretion through renal clearance after therapy.[19] Herein, we report a SAN-conjugate-based combination cancer therapy that exploits the sophisticated concertion of spatiotemporal therapeutic actions at the cellular (and subcellular) level, yielding a therapeutic efficacy that is enhanced by nearly an order of magnitude when compared with sequential or independent treatments. As a result, the effective dosage can be lowered to a level at which neither of the individual components reaches the therapeutic efficacy. The cancer targeting was observed at the cellular level *in vitro*, and remarkably, the targeting effect was found to extend to the organ and whole body levels *in vivo*. With the specificity and spatiotemporal concertion of these two therapeutic actions, significant tumor growth suppression was demonstrated in the animal model.

RESULTS AND DISCUSSION

Dual Function of Smart Gold Nanoparticle Conjugates for Drug Delivery and Photothermal Therapy. SANs were modified to act as a photothermal therapeutic agent and as a delivery vehicle for chemo agents, as well (Figure 1). Our conjugate system consists of SANs and chemo agents that are covalently linked at the terminals of the SAN surface ligands. The SAN conjugate is designed to release the chemo agents and simultaneously form aggregates of the Au nanoparticles (Au NPs) in a mildly acidic environment. Both chemo and thermo therapeutic actions can be triggered by the pH change in the intracellular environments of cancerous cells.[20,21] We hypothesized that this combination therapy can be more selective for cancer than conventional drugs because it is a pH-controlled drug release system. In addition, the Au NPs can conditionally utilize external light by their aggregation-induced absorption shift. SANs were prepared according to the method described in our previous report.[9] Doxorubicin (Dox), one of the most common anticancer agents in clinical use,[22] was used as a model chemotherapeutic. Dox molecules were covalently linked to SANs *via* carbodiimide coupling to yield SAN−Dox conjugates (abbreviated as SANDCs) (see Methods for the conjugation procedure). Typically, tens of Dox molecules were conjugated per SAN by careful control of the reaction ratio. This allows a considerable proportion of the initial SAN ligand to remain unchanged in the resultant SANDCs. Under mildly acidic conditions, hydrolysis-induced cleavage of the ligand linker can result in the release of the Dox molecules. At the same time, the SANDC surface ligands, irrespective of whether they are Dox conjugated, begin to reveal positive surface charges. This exposure induces rapid aggregation of the Au NPs through the electrostatic interactions between surfaces bearing both positive and negative charges. The optical properties of the SANs remained unchanged after the Dox conjugation, and no noticeable change in their hydrodynamic size was observed (Supporting Information Figure S1). The pH-responsive Dox release and aggregate formation of SANDCs have been studied in buffer solutions with the pH level of 2.0, 5.5, or 7.4. The samples in the pH 2.0 and pH 5.5 environments showed a red shift and broadening of their absorption band over time, and the pH 2.0 sample showed a more rapid change than the pH 5.5 sample (Figure 2a,b). The red shift and broadening are ascribed to the appearance of coupled plasmon modes and the inhomogeneity of the aggregates.[9] The pH 7.4 sample, however, showed no noticeable absorption change (Figure 2c). Hydrodynamic sizes and zeta-potentials were concurrently measured over time for the SANDC samples at different pH (Figure 2d,e). In pH 2.0, the hydrodynamic size rapidly increased to ~250 nm within 5 min, and the pH 5.5 sample showed slower

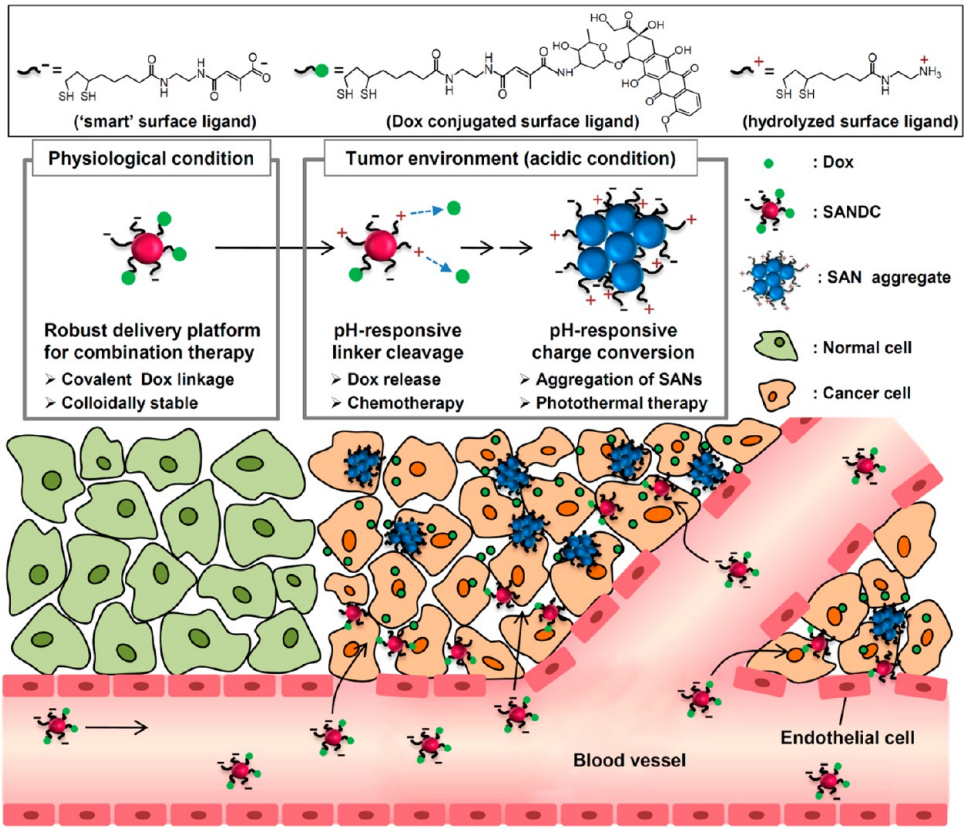

Figure 1. Schematic illustration of the working mechanism of "smart" gold nanoparticle doxorubicin conjugate (SANDC). SANDC consists of smart gold nanoparticles (SANs) and covalently conjugated doxorubicin (Dox). The SANDC is designed to release the Dox by pH-triggered linker cleavage under the mild acidic conditions in tumor. Simultaneously, the SANDC is designed to convert the surface charge from negative to a mixture of negative and positive charges, which induces rapid aggregation among the nanoparticles *via* electrostatic interactions. This spatiotemporally concerted release from SANDCs is exploited for chemo and photothermal combination cancer therapy.

increase. Zeta-potential measurements coincided with the hydrodynamic size change. The pH 2.0 sample showed most rapid change in the zeta-potential value as the SANDC surface charge was converted from negative to positive. The pH 5.5 sample showed slower change in the zeta-potential. No noticeable changes were found for the pH 7.4 sample neither in the hydrodynamic size nor in the zeta-potential. Time evolution of the SANDC aggregates was directly observed by TEM, which confirms the pH-dependent growth of aggregates over time (Figure 2g). The pH 7.4 sample did not show any change over time under TEM (data not shown). The absorption shift, hydrodynamic size, zeta-potential, and TEM measurements all consistently confirm pH-induced aggregation of SANDCs. The pH-responsive release profile of Dox molecules from the SANDCs was monitored by following the Dox fluorescence (Figure 2f). Initially, all three samples showed negligible emission from the conjugated Dox molecules because their fluorescence was effectively quenched in close proximity to the Au NPs. The pH 2.0 and pH 5.5 samples showed an initial "burst" of fluorescence intensity from the released Dox molecules in 5 min, after which the intensity plateaued. The pH 2.0 sample showed a more rapid release of Dox than did the pH 5.5 sample, which coincides with the Au NP aggregation behavior. The Dox release at pH 5.5 is not high, presumably because of the fast Au NP aggregations, which impedes further hydrolysis and subsequent release of the Dox by reducing effective surface areas. In compartmentalized environments such as in cells, the release can be more rapid and efficient because the compartment limits the formation of huge aggregates. The observed pH-dependent changes in the SANDCs are caused by pH-dependent hydrolysis of the citraconic amide linker in the surface ligand,[23−25] which is effectively transduced into the release of the conjugated Dox molecules from the SANDCs and the formation of aggregates of the Au NPs.

Spatiotemporal Concertion of the Combination Modalities. Since the pH-induced Dox release and Au NP aggregation were confirmed for SANDCs, we further applied them in cellular applications. Most cells, especially the cancerous ones (including B16 F10 mouse melanoma cells), are known to engulf nanoparticles *via* energy-dependent and energy-independent pathways.[26,27] B16 F10 cells were coincubated with 20 nM SANDC that contained 20 Dox per Au NP. As controls, cells were also treated with physical mixture of 20 nM SAN and 400 nM Dox (abbreviated as SAN&D), 400 nM Dox,

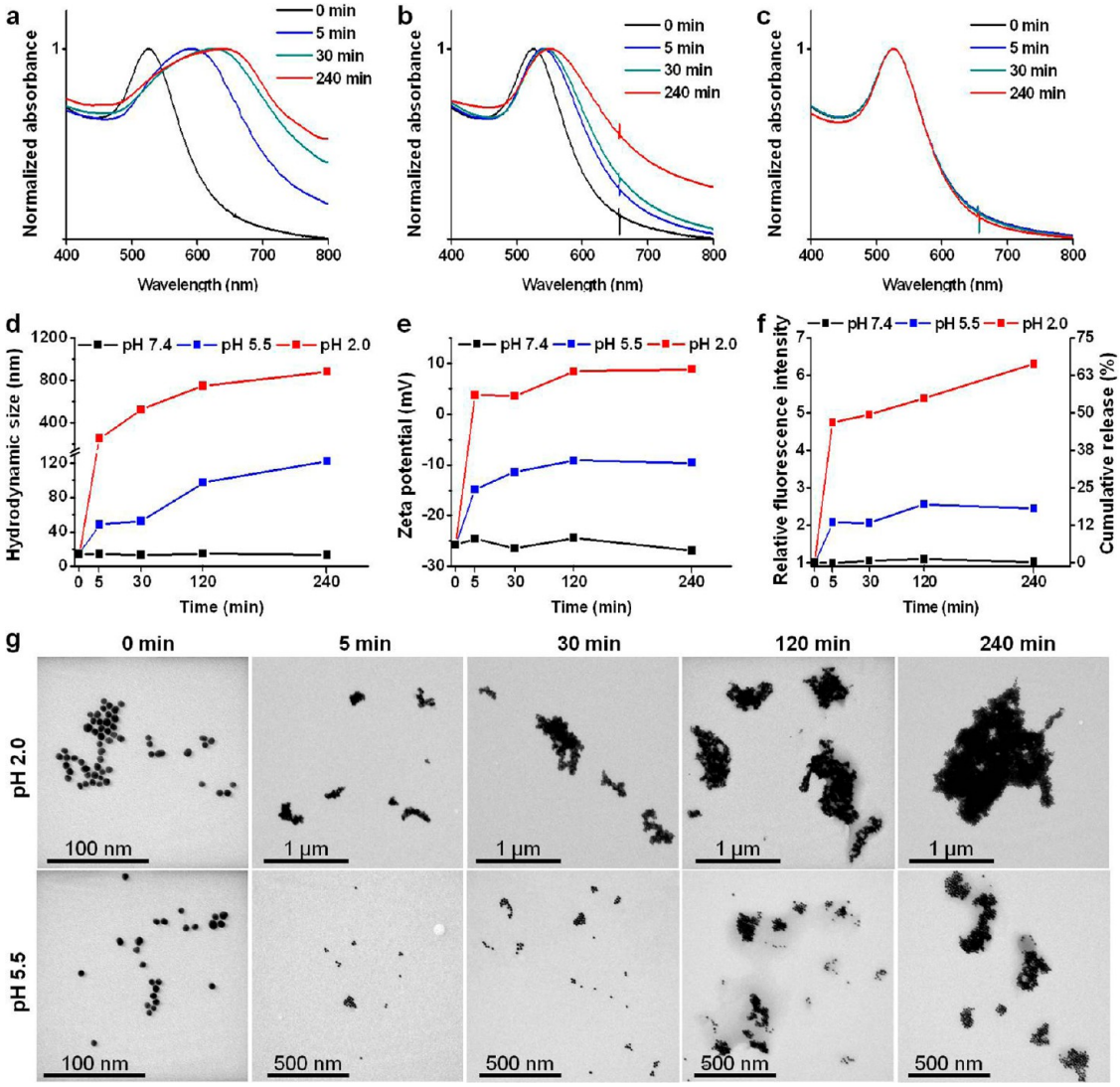

Figure 2. pH-induced aggregation of gold nanoparticles and simultaneous Dox release. (a–c) Time evolution of absorption for SANDC in pH 2.0 (a), pH 5.5 (b), and pH 7.4 (c) aqueous solutions. (d–f) Hydrodynamic size (d), zeta-potential (e), and relative fluorescence intensities (scale on the left axis) and percentages of cumulative release (scale on the right axis) of Dox (f) for SANDC at different elapsed times in different pH levels. (g) TEM images showing the aggregates of SANDCs in pH 2.0 (top) and pH 5.5 (bottom) samples at different elapsed times.

and 20 nM SAN, respectively. The SANDC sample showed a gradual and continued release of Dox, which appeared red in the fluorescence images (Figure 3a). The control SAN&D and Dox samples showed noticeable fluorescence as early as at 1 h. The SAN sample, which did not have any Dox, showed no fluorescence. The Dox fluorescence intensity was quantified by the signal to background ratio (SBR) (Figure 3b) (see Supporting Information for details).[28,29] The SANDC sample showed the slow and monotonic increase in SBR, which indicates the sustained release of Dox from the SANDCs by the pH-induced hydrolysis. In the case of SAN&D and Dox control, the SBRs showed a similar pattern: an initial rapid increase, reached the maximum value after 6 h, and decreased. This pattern suggests an efficient efflux following the rapid uptake of Dox molecules and also suggests that the cellular uptake and distribution of Dox was not affected by the simple coexistence of SAN. For the SANDC, SAN&D, and Dox samples, viability levels were monitored (Figure 3c). After 48 h, the three samples showed a similar viability level. SAN sample was used for control and showed the high viability level at all times, which indicates negligible toxicity of SAN in the absence of external light. Dark-field microscopy revealed efficient accumulations of Au NPs inside the cells (Figure 3a). The SANDC, SAN&D, and SAN samples showed an increase in scattering over time with strong orange color, which allowed partial visualization of the cellular morphologies. However, the intracellular distributions of the scatterers seemed to be not identical. The scattering was more centered at nuclei for the SANDC sample, whereas SAN&D and SAN samples have the scattering broadly distributed in the cytoplasm (additional dark-

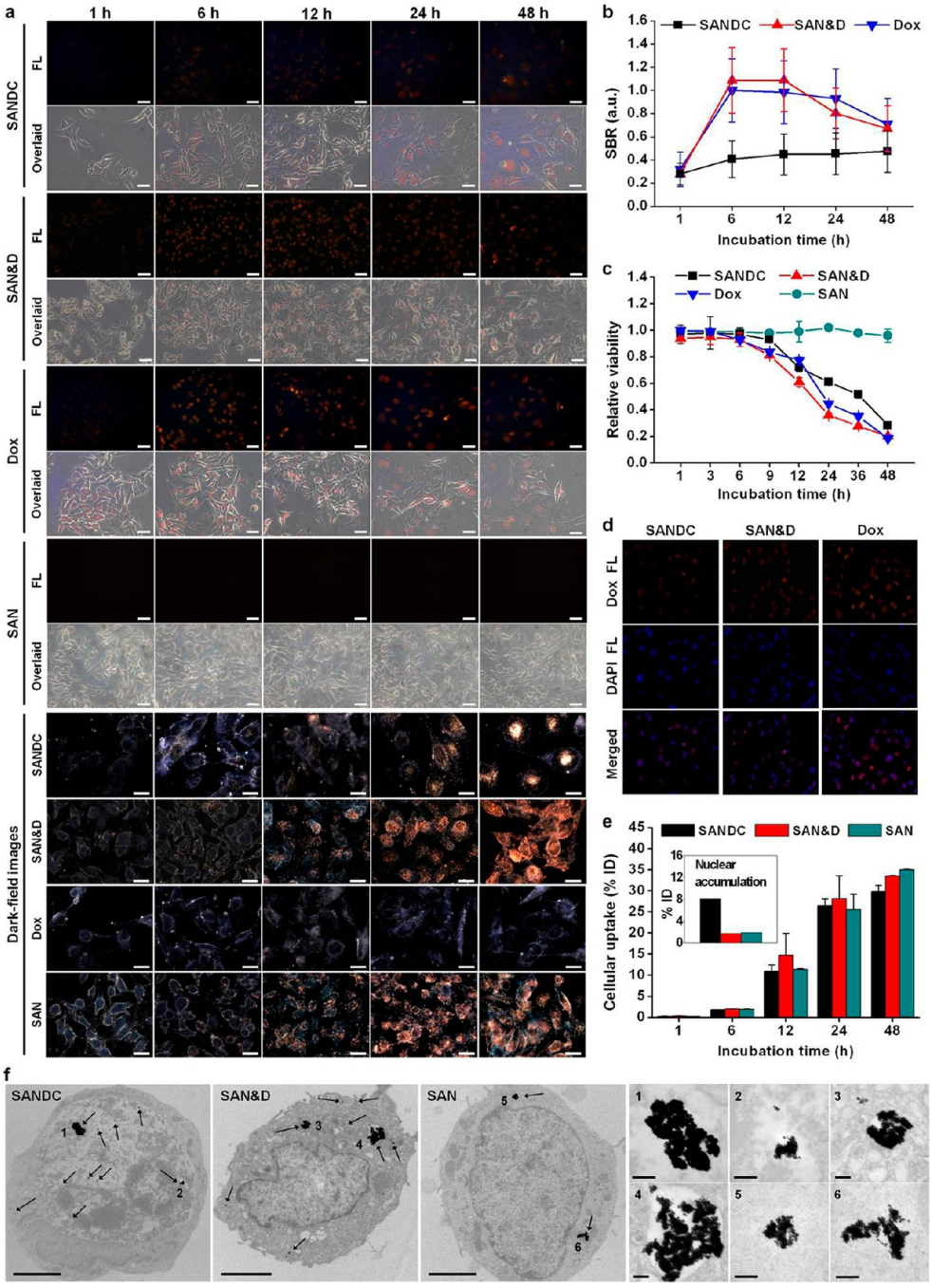

Figure 3. Spatiotemporally concerted actions of SANDCs at the cellular level. (a) (Top) Fluorescence images (FL) and their overlays with phase-contrast images (overlaid) for cells treated with SANDC, SAN&D, Dox, or SAN (scale bars: 40 μm). (Bottom) Dark-field microscope images (scale bars: 20 μm). (b) Signal to background ratios determined from the fluorescence microscope images. (c) Relative viability levels in dark condition. (d) Fluorescence images after colabeling with DAPI for the cells coincubated with SANDC, SAN&D, or Dox. (e) Cellular uptake of gold nanoparticles measured by ICP-AES after coincubation of cells with SANDC, SAN&D, or SAN. Inset shows the nuclear accumulation levels after 24 h coincubation. (f) (Left) Sectioned TEM images showing the intracellular localization of gold nanoparticles after coincubations of cells with SANDC, SAN&D, or SAN (scale bars: 3 μm). The arrows indicate the gold nanoparticle aggregates. (Right) Magnified images of the representative aggregates (1−6) from the left (scale bars: 200 nm).

field images can be found in Supporting Information Figure S2). The dark-field images suggest translocations of SANDC into the nuclear region, and the images are also similar to other nuclear-targeting Au NP cases.[30] To follow the intracellular distribution of the released Dox from the SANDCs, nuclear staining was performed using 4′,6-diamidino-2-phenylindole (DAPI). Colocalization was observed between the released Dox fluorescence from SANDCs and the DAPI-stained nuclei (Figure 3d). The intracellular distribution of the released Dox from SANDC was similar to that of the control SAN&D and Dox samples. The Dox from the SANDC may

have entered the nuclei after its release. The tethered Dox may have directed the translocation of SANDCs to the nuclei. Using inductively coupled plasma atomic emission spectrometry (ICP-AES), cellular uptake of Au NPs was quantitatively measured for the SANDC, SAN&D, and SAN samples. They showed similar cellular accumulation level of percentage incubated dose (% ID) reaching ~30% after 48 h (Figure 3e). For each sample, the cell nuclei were isolated at 24 h and the %ID in nuclei was quantified by ICP-AES (inset in Figure 3e; see Methods for details). The SANDC sample showed significant nuclear accumulations with the %ID as high as 8%, which consisted of ~30% of the total Au NP accumulation. It was also over 4-fold larger than that of SAN&D (1.7%) or SAN (1.9%). The SANDC translocation into cell nuclei was further confirmed by resin−section TEM studies (Figure 3f). For the SANDC sample, many Au NP aggregates were found in the nuclear region along with some aggregates in the cytoplasm, which confirmed nuclear translocation of the SANDCs. In contrast, the Au NP aggregates were found exclusively in the cytoplasm for the SAN&D and SAN samples. An active nuclear translocation mechanism has been proposed for Dox, in which Dox forms a Dox−proteasome complex in the cytoplasm and translocates into the nucleus *via* nuclear pores.[31] This translocation could occur for single Au NPs or small Au NP aggregates because nuclear pore transportation is limited to a hydrodynamic size of less than 100 nm.[32,33] Alternatively, larger aggregates may gain access to the nucleus when the nuclear envelope is fragmented into subcomplexes during mitosis.[34] The aggregation of SANDCs is expected to continue after their internalization into the nucleus; therefore, the size of the aggregates determined by TEM may not represent their actual size at the time of internalization. SANDC showed massive cellular accumulations *via* the aggregation-based accumulations, and the Dox conjugation resulted in the effective translocation of Au NP and Dox to the cell nuclei. In SANDC, the Au NP and conjugated Dox overlap each other spatiotemporally in their cell entry and also significantly within the intracellular compartments.

Highly Synergistic Efficacy at the Cellular Level. SANDC shows spatiotemporally overlapping accumulation of Dox and Au NP aggregates in the cell nuclei. This simultaneous accumulation can be beneficial for highly synergistic cancer therapy. B16 F10 cells were co-incubated with SANDCs. Each SANDC was conjugated with, on average, one Dox molecule (denoted SANDC-1, where the number indicates the equivalent number of conjugated Dox per Au NP). For control samples, Dox, SAN, and SAN&D-1 were used. The concentrations were matched at 20 nM for the Au NP and Dox. After 9 h, the cells were irradiated with a 660 nm cw diode laser (8 W/cm^2) for 1 min. Only the SANDC-1 sample showed a significant viability reduction to 50%, while the other samples showed negligible changes in their viabilities (Figure 4a). The SAN&D-1 sample showed negligible cytotoxicity despite having received identical doses of Dox and Au NPs as the SANDC-1 sample. The spatiotemporal concertion of the SANDCs is thought to produce the enhanced cytotoxicity. Viability changes in dark conditions were evaluated for the SANDC-1 and control Dox sample (Figure 4b). Up to 2 days, no noticeable cytotoxicity was found for either sample. A Dox concentration of 20 nM did not reach the level for effective cytotoxicity. Dox concentrations of 20, 200, 400, and 800 nM were co-incubated for 9 h, and the cells were laser irradiated (8 W/cm^2) for 0 (no exposure), 1, 3, 5, and 10 min. Within the Dox concentration range and irradiation time, the cells retained over 80% of their viability (Figure 4c). An increase in the Dox concentration to 800 nM did not cause a significant reduction in the cell viability level. As another control, the experiment was repeated using 20 nM 11-mercaptoundecanoic acid (MUA)-capped Au NPs conjugated with 40 Dox per Au NP (denoted as MANDC-40). The cells retained high viability levels over 80% throughout the irradiation up to 10 min. This indicates that the formation of Au NP aggregates is essential to show the photothermal cell destroying effect. Based on this result, 20 nM SANDC-1, SANDC-10, SANDC-20, and SANDC-40 samples were prepared to demonstrate the synergistic effect (Figure 4d). A 20 nM SAN sample was used as a control. As expected, all of the SANDC samples and the control SAN sample retained the high viability levels prior to the laser irradiation. After 1 min of laser irradiation, the cell viability was strongly dependent on the degree of Dox conjugation. The SANDCs with higher Dox conjugation levels showed greater reductions in the post-irradiation viability level. The SAN control retained the highest viability level. Neither 20 nM SAN nor 800 nM Dox alone exhibited significant cytotoxicity. However, 20 nM SANDCs did show effective cytotoxicity. This result clearly demonstrates the synergistic effect of the SANDCs. After 3 min of irradiation, the viability levels of all of the SANDC samples decreased to less than 10%. The 3 min irradiation also resulted in a significant cytotoxicity for the SAN sample. As the irradiation time was increased to 5 and 10 min, the viability levels decreased further, and the differences among the SANDC samples and between the SANDCs and the control SAN became smaller. These increasingly comparable results are attributed to the dominance of the Au NP photothermal effect under longer irradiation times. The experiments were repeated using unconjugated mixture controls of 20 nM SAN&D-1, SAN&D-10, SAN&D-20, and SAN&D-40 samples (Figure 4e). Contrary to the SANDC cases, SAN&D samples showed the viability levels that were not depending on Dox concentration irrespective of the irradiation time. SAN&D samples

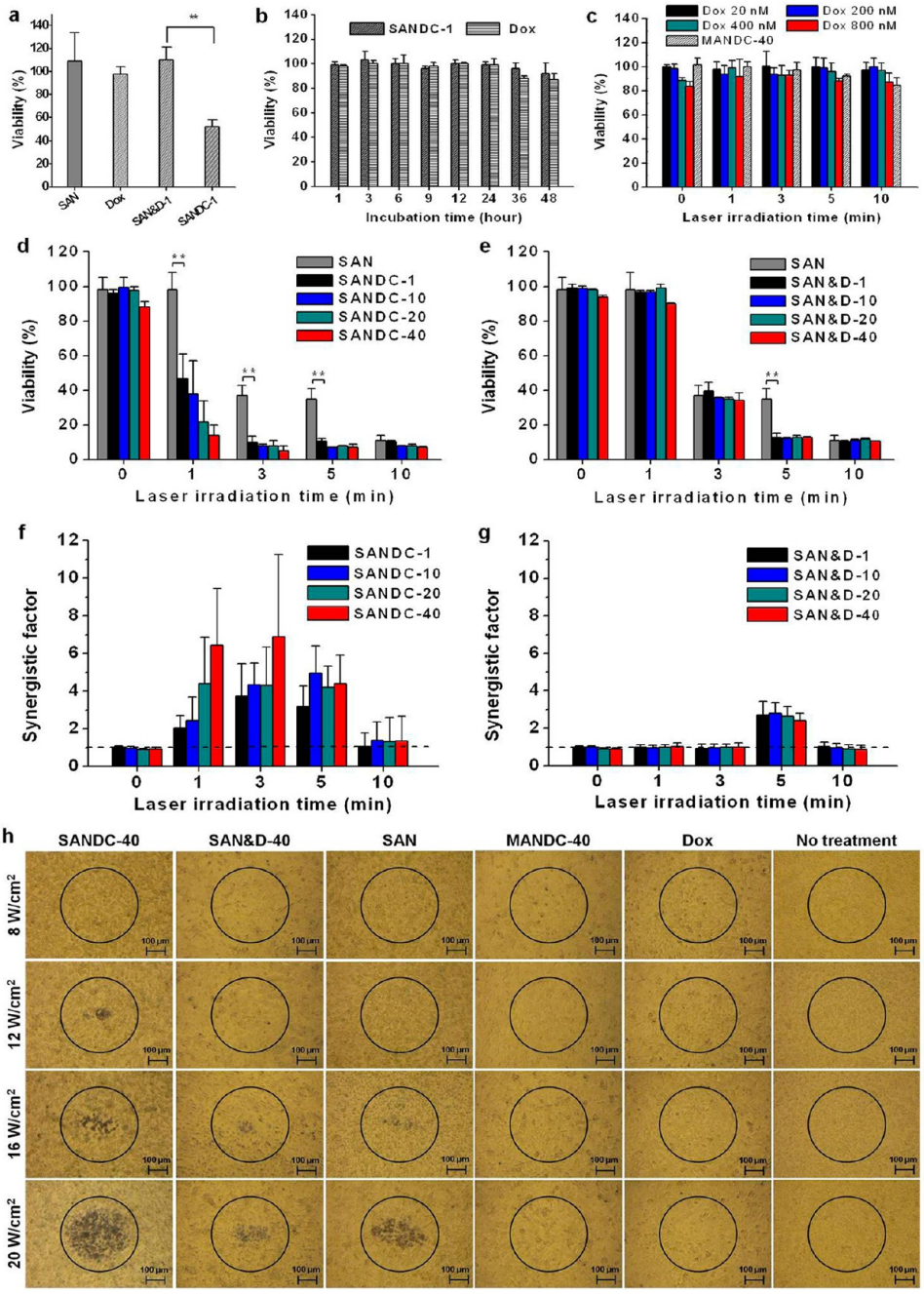

Figure 4. Evaluation of synergistic efficacy of SANDC combination therapy at the cellular level. (a) Viabilities of cells after their coincubation with SAN, Dox, SAN&D-1, or SANDC-1 and subsequent laser irradiation for 1 min ($P = 0.0014$). (b) Viabilities without laser irradiation for the cells treated with SANDC-1 or Dox. (c) Viabilities of the cells coincubated with various concentrations of Dox or MANDC-40 and exposed to laser irradiation. (d,e) Viabilities of the cells coincubated with SANDCs with different Dox conjugation levels (d) or with SAN&Ds with different Dox concentrations (e) and exposed to laser irradiation (**$P < 0.01$). (f,g) Synergistic factors for the SANDCs (f) and SAN&Ds (g). The dashed lines represent the synergistic factor level of 1. (h) Photothermal destruction of the cells co-incubated with SANDC-40, SAN&D-40, SAN, MANDC-40, Dox, or no treatment for 24 h followed by laser irradiation for 5 min at different power densities. Trypan blue was used to reveal the dead cells with blue staining, and circles denote the position of the laser spot.**

showed similar viability levels as those of the SAN control sample except for the case of 5 min irradiation which was the only case that showed meaningful synergistic effect. SAN&D samples showed significantly less efficient cell destroying effect when compared with SANDC samples. For an example, the SAN&D-40 sample showed the reduction of viability to 13% after 5 min irradiation, where a similar level was achieved within 1 min irradiation by SANDC-40 sample.

To reveal the synergistic effect, synergistic factors were obtained by dividing the predicted additive viability by the viability after the combination therapy (Figure 4f). The additive viability is obtained from the expression $V_{Additive} = V_{Chemo} \times V_{Thermo}$, where $V_{Additive}$

is the predicted viability as a result of the purely additive interaction between the chemo and thermo therapies, and V_{Chemo} and V_{Thermo} are the viabilities after the chemo and thermo therapies alone, respectively.[1,12] The synergistic factors were ~1 for all samples prior to laser irradiation, which indicates the absence of any synergistic effect. The largest synergistic factor, a value of 6.9, was obtained for the SANDC-40 sample after 3 min of laser irradiation. After 10 min irradiation, the synergistic factors were reduced back to ~1. This trend indicates that a balanced treatment is necessary to achieve maximal synergistic interaction between the two modalities. The synergistic factor of ~7 is higher than that observed in previous combination treatments using gold nanostructures, in which the maximal synergistic factors were ~4 for cisplatin[12] and ~2 for Dox.[13,14] On the other hand, SAN&D samples showed the synergistic factors of 1 for the most cases except the 5 min irradiation case with the highest synergistic factor of 2.8 (Figure 4g). As shown in Figure 3, SAN&D showed similar cellular uptake level and Au NP aggregates formation capability as SANDC. The only major difference lies in the subcellular distribution. SANDC delivers the Au NP aggregates to cell nuclei, which can induce effective spatiotemporal overlaps with Dox. This spatiotemporal concertion is thought to yield the large synergistic factor of SANDC over SAN&D. This concertion also reduced the chemo and thermo agent dosages to a level at which sequential treatments did not show meaningful efficacy. This dose reduction may be important for clinical cancer therapy because it may alleviate dose-dependent systemic side effects. For example, Dox is known for its cardio-toxicity, which is one of the main challenges in its clinical use.[22] The ability to reduce the dosage while retaining efficacy could extend the chemotherapeutic window and minimize the side effects of the treatment.

The synergistic effect of SANDCs can be explained by the enhanced cytotoxicity of Dox at a locally elevated temperature. Conversely, the conjugated Dox can be thought to enhance the photothermal cytotoxicity of Au NPs. Photothermal therapy using SAN typically exhibits a threshold behavior for the laser intensity.[9] The threshold behaviors were studied for 20 nM SANDC-40, SAN&D-40, SAN, MANDC-40, and 800 nM Dox samples. After 24 h of co-incubation, the B16 F10 cells were exposed to laser irradiation for 5 min, and the laser intensity was varied from 8 to 20 W/cm^2 (Figure 4h). Trypan blue was used to reveal the cell mortality. SANDC-40 showed the photothermally effective laser power threshold lower than 12 W/cm^2, while the control SAN&D-40 and SAN samples showed the cell mortality at a laser power of ~16 W/cm^2. This threshold reduction of SANDC clearly demonstrates the enhanced photothermal cytotoxicity by the synergistic effect. For the other control experiments using MANDC-40, Dox, or only cell growth medium (denoted as "no treatment"), no mortal cells were found within the laser power range. Dox has multiple modes of action, such as inhibition of DNA and RNA synthesis by intercalating into DNA and binding to topoisomerase II, generation of free radicals, and directing DNA damage by alkylation.[27] Thermal chemopotentiation of Dox may be related to the increase in the DNA damage caused by the drug, such as double-strand breaks by DNA alkylation and the inhibition of DNA replication and repair by denaturation of nuclear proteins.[2,3] SANDCs can accumulate in the cell nucleus region and locally generate heat upon excitation by external light. This nuclear-localized heating can effectively enhance the DNA damage caused by Dox. In addition, the nuclear accumulation of Au NPs may itself cause cytotoxic DNA double-strand breaks, which can increase the therapeutic efficacy.[30]

Smart Gold Nanoparticles Target Cancer at the Cellular and Organ Levels. As a control Au NP for comparison to SAN, a MUA-capped Au NP (abbreviated as MAN) was prepared. The SANs and control MANs were synthesized using identical Au NP cores, and they exhibited similar absorption profiles (Supporting Information Figure S3), hydrodynamic size (~14 nm), and surface charge (zeta-potential of ~ −35 mV). MAN can provide surface properties similar to those of SAN but does not contain a hydrolysis-susceptible linker and, as a result, does not show pH-dependent surface charge conversion and the subsequent aggregations.[9] SANs can exhibit enhanced cellular accumulations, especially for cancerous cells. SANs and MANs were each co-incubated with B16 F10 cells and NIH 3T3 mouse embryonic fibroblast cells (normal control cell against B16 F10 cells). After 24 h, the samples were examined by dark-field microscopy. The SANs accumulated very efficiently in B16 F10 cells while only in a moderate level in the normal control cell case (Figure 5a). In contrast, the MANs showed almost no scattering for either the B16 F10 or the NIH 3T3 cells. After SANs are internalized into cells, they form aggregates and accumulate in the cell interior. As they form aggregates, exocytosis should be effectively blocked by their increased size. Because cancerous cells are more phagocytic, SAN and SANDC can selectively accumulate in cancer cells, showing cancer targeting effect without any targeting moieties. In contrast, MANs do not exhibit such cancer specificity because they lack the aggregation capability of the SANs; MAN/MANDC can form aggregates only at pH lower than 4.0, which is ascribed to the protonation of carboxylic acid groups (Supporting Information Figure S4). To investigate if such cancer targeting effect can continue in *in vivo* organ level, biodistributions of SAN, SANDC-40, and MAN were studied using animal model with nu/nu nude mice bearing B16 F10 melanoma cells grafted onto the flank (Figure 5b−d). The percentages of Au NPs localized in major organs and in the

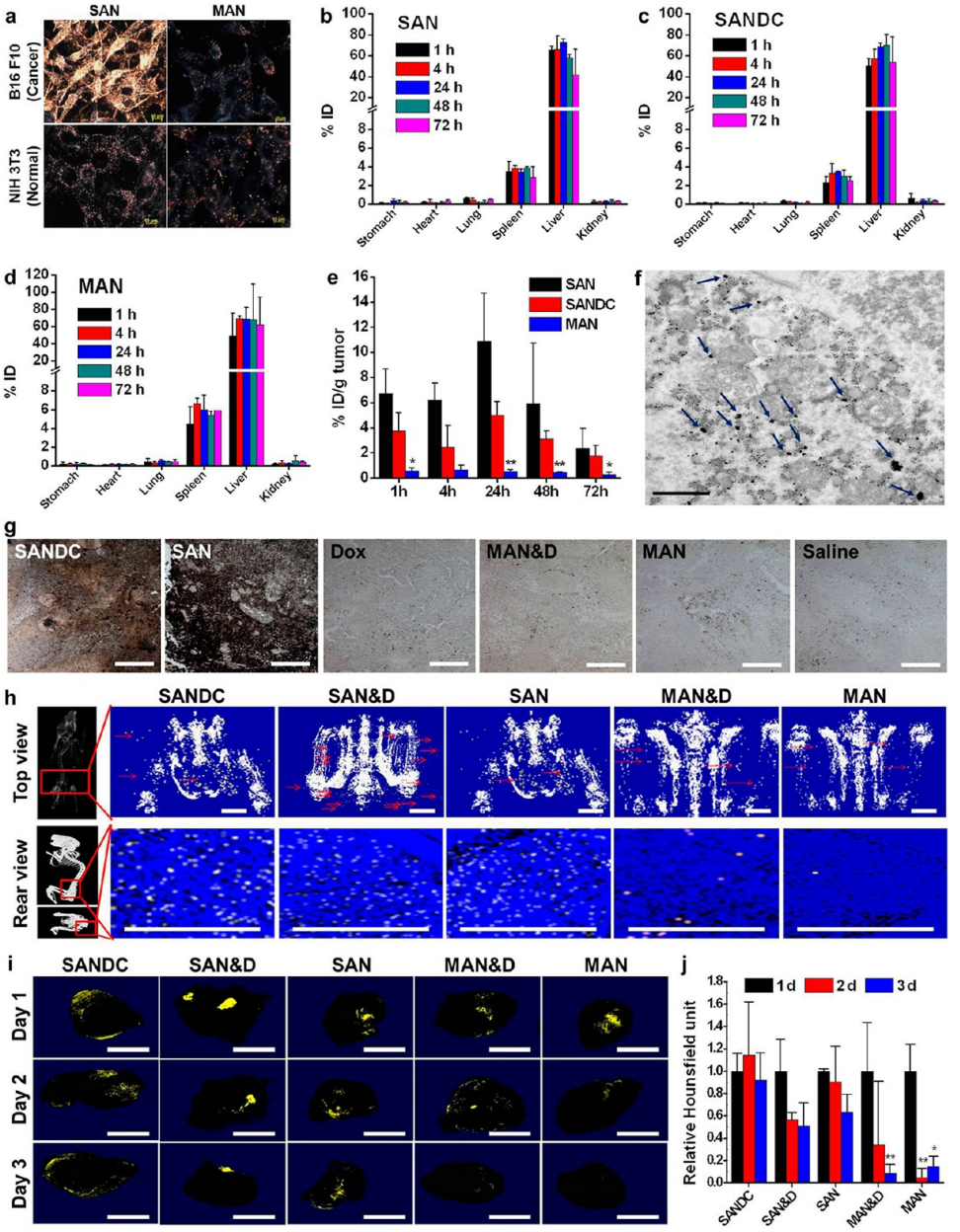

Figure 5. SANDC accumulation in cancer at cellular and organ levels. (a) Dark-field microscopic images of B16 F10 (cancer) cells and NIH 3T3 (normal) cells co-incubated with SAN or MAN. (b–d) Biodistributions of SAN (b), SANDC (c), and MAN (d) in the major organs measured by ICP-AES after 1, 4, 24, 48, or 72 h intravenous injection into tumor-bearing mice (n = 3). (e) Tumor accumulation levels of SAN, SANDC, and MAN (*P < 0.05 and **P < 0.01 compared to SANDC group). (f) TEM image of tumor tissue retrieved at 24 h intravenous injection of SAN. Arrows indicate gold nanoparticle aggregates (scale bar: 1 μm). (g) Optical microscope images after silver enhancement staining of tumor tissues sectioned 24 h after intravenous injections (scale bars: 100 μm). (h) *In vivo* whole-body CT imaging for tumor accumulation at 3 day after the intravenous injection. White indicates the bones, and dots (red arrows) indicate the gold nanoparticles (scale bars: 10 mm). (i,j) CT images (i) and corresponding accumulation levels of gold nanoparticles in relative Hounsfield unit (j) in the tumor at 1, 2, and 3 day after intratumoral injections. Yellow indicates gold nanoparticles in the tumor (scale bars: 10 mm). Hounsfield units are normalized to that of 1 day (*P < 0.05 and **P < 0.01 compared to SAN group).

tumor were measured by ICP-AES at 1, 4, 24, 48, and 72 h after intravenous injection of 1 μM SAN, SANDC, or MAN PBS solution. In the major organs, similar biodistribution patterns were found for all samples, showing large accumulations of the Au NPs in the organs of reticuloendothelial system (RES; *e.g.*, liver, spleen) together with the %ID ranging from 50 to 80%. This pattern is similar to previously reported biodistributions for negatively charged NPs with the hydrodynamic size over 10 nm.[35,36] As for the tumor accumulation, SAN and SANDC showed significantly higher accumulations in tumor when compared with MAN. SANs have accumulated in the tumor most rapidly with the peak accumulation at 24 h showing the injected dose per gram of tumor (% ID/g) as high as 10.9% (Figure 5e). SANDC showed the highest tumor accumulation of 5.0% ID/g

at 24 h. The control MAN showed significantly smaller tumor accumulations when compared with the cases of SAN or SANDC at all circulation times (Supporting Information Figure S5). The highest accumulation of MAN was 0.64% ID/g at 4 h, which is 17 times smaller than that of SAN at 24 h. It is remarkable that, despite the trapping in RES organs, SANs and SANDCs showed comparable tumor accumulation levels to the cases of larger and antifouling surface-coated NPs such as polyethylene glycol-decorated NPs.[8,17,37,38] The high tumor accumulation of SANs and SANDCs is thought to result from the efficient permeation into tumor by the small size and their slow clearance from the tumor region by their aggregation capability. Small and negatively charged NPs, like SAN and SANDC, can rapidly diffuse into tumor extracellular matrix and penetrate deep into tissues.[39] Once permeated, NPs with the small hydrodynamic size should be rapidly cleared from the interstitial space of tumor; however, large NP aggregates can effectively accumulate in the tumor region.[40] To simulate the pH-induced aggregations *in vivo*, SAN and SANDC were monitored in 100% fetal bovine serum (FBS). When SAN and SANDC were each incubated in pH 5.5 FBS at 37 °C, both samples showed the formation of Au NP aggregates as confirmed by the absorption shift, hydrodynamic size, and TEM measurements (Supporting Information Figure S6). In neutral pH FBS at 37 °C, both SAN and SANDC samples retained the colloidal stability. The formation of Au NP aggregates was pH-responsive and not from simply losing the colloidal stability. The colloidal stability is necessary for effective tumor permeation because extravasation of large aggregates should be limited by the transvascular pore barriers in the vessel wall.[41] To exclude the possibility that control MAN/MANDC lose the colloidal stability in dilution medium or *in vivo* environment and fail to permeate into the tumor, their colloidal stability was studied by monitoring the absorption changes in PBS and FBS. No noticeable changes in absorption were found up to 24 h, indicating the colloidal stability in *in vivo* (Supporting Information Figure S7). At the cellular level, SANs or SANDCs can easily enter cancer cells because of their relatively small size and can accumulate in the cancer cells by effectively blocking the exocytosis. Their relatively small size also allows them to permeate effectively into a tumor region. After they are extravasated into the tumor interstitial space, they accumulate in the region as aggregate and increase their size. The aggregation of SANs in the tumor region was directly confirmed by TEM (Figure 5f). The tumor was dissected at 24 h after intravenous injection, and the tissue was embedded with epoxy resin and sectioned. Many aggregates of SANs were observed, some of which were as large as 200 nm, which is similar to the size of aggregates found in acidic FBS medium shown in Figure S5. Following types of Au NPs were intravenously injected into mice: SAN, SANDC-40, SAN&D-40, MAN, and physical mixture of MAN and Dox (abbreviated as MAN&D-40). Saline and Dox were used as control. At 24 h post-injection, the tumor tissues were excised and enhanced by silver staining for microscopic histological examination. The silver staining revealed large accumulations of Au NPs in the cases of the SANs and SANDCs (Figure 5g). In contrast, no appreciable silver staining was observed for the MANs and MAN&Ds; their staining level was comparable to the control cases of Dox and saline. The fixed tumor tissues at 24 h post-injection were also imaged by the micro-CT system (Supporting Information Figure S8). Many Au NPs were found in the fixed tissues of the SAN, SANDC, and SAN&D cases, confirmed by the high levels of X-ray scattering. This CT results coincide with those of the silver staining experiment. *In vivo* whole-body CT imaging was also performed to further confirm the tumor accumulation of different types of Au NPs. The *in vivo* CT analysis showed that the intravenously injected SAN, SANDC, and SAN&D were more accumulated in the tumor region than MAN and MAN&D at 3 day post-intravenous injections (Figure 5h). The Hounsfield unit in the tumor region quantitatively showed the higher accumulation of SAN, SANDC, and SAN&D over MAN&D and MAN (Supporting Information Figure S9). To demonstrate the slow clearance of SAN and SANDC *in vivo* and verify their high accumulations in tumor, their accumulations in a well-established tumor were evaluated through CT analysis after intratumoral injections. CT analysis of the tumors that were surgically retrieved on day 1, 2, and 3 after the intratumoral injection of different types of Au NPs showed that SANDC, SAN, and SAN&D remained more efficiently than MAN and MAN&D in the tumor region, showing a slower clearance rate from the tumor (Figure 5i). The accumulation levels of each sample in the tumor were quantified using Hounsfield unit (Figure 5j). SAN, SAN&D, and SANDC can aggregate in tumor and increase the size of the aggregates. This is thought to result in the effective accumulation and high retention of the NPs in the tumor by their slow clearance from the tumor region.

Tumor Suppression at the Whole-Body Level. Aggregated Au NPs in a tumor can generate heat shock upon irradiation with external light. To monitor the heat generation, the local temperature increase in the tumor was measured during laser irradiation (660 nm, 0.5 W/cm^2). SANDC-40, SAN&D-40, SAN, Dox, MAN&D-40, MAN, and saline were intravenously injected into mice. At 24 h post-injection, a thermocouple needle was inserted into the tumor region, and the local temperature was measured for the 5 min duration of the laser irradiation and for 3 min post-irradiation (Figure 6a). The SAN, SAN&D, and SANDC samples showed a similar rapid increase in their temperature (by an increment of ~15 °C). After laser irradiation, the temperature quickly

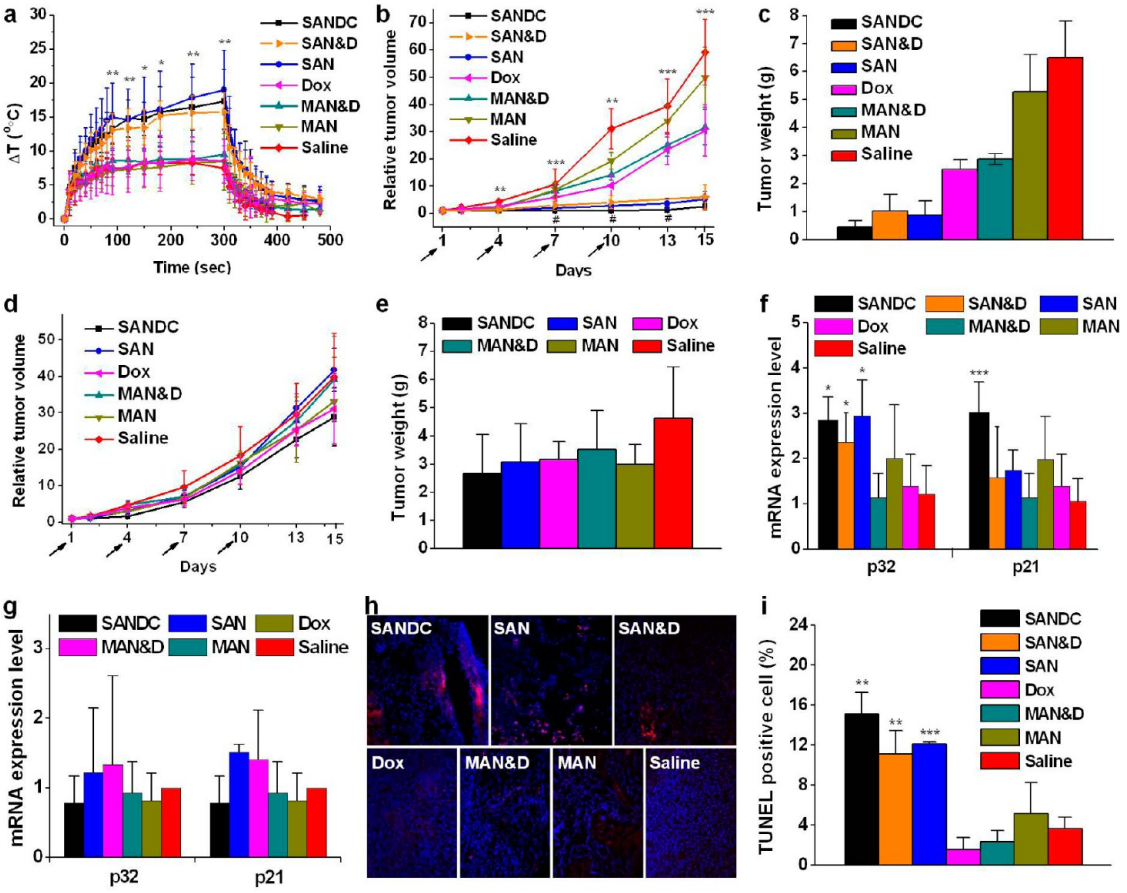

Figure 6. Tumor suppression at the whole-body level. (a) Local temperature of tumor core during and after the laser irradiations ($n \geq 4$). *$P < 0.05$ and **$P < 0.005$ are noted between SAN and saline. (b–e) Relative tumor volume changes over 15 days with (b) or without (d) repeated laser irradiations ($n \geq 6$). The arrows indicate injection time points (day 1, 4, 7, and 10). **$P < 0.005$ and ***$P < 0.001$ are noted between SAN and Dox. $^{\#}P < 0.05$ is noted between SANDC and SAN. On day 15, final tumor mass was measured for the case of repeated laser irradiations (c) and for the case of no laser exposure (e). (f,g) qRT-PCR results of p21 and p32 protein expression levels of tumor tissues after repeated laser irradiations (f) or after no laser irradiation (g) ($n = 5$). *$P < 0.05$ and ***$P < 0.001$ for comparison with saline control. (h,i) TUNEL and DAPI-stained images of tumor tissues (h) and the TUNEL-positive cell percentages (i) (scale bars: 200 μm). **$P < 0.005$ and ***$P < 0.001$ for comparison with Dox, MAN&D, MAN, and saline.

returned to its ambient temperature, which indicates the efficient dissipation of heat into the surroundings of the locally heated area. The MAN and MAN&D controls showed temperature profiles that were very similar to the cases of the control Dox and saline. This set of results demonstrates the high photothermal conversion efficiency of SANs, SAN&Ds, and SANDCs. They can efficiently form aggregates in tumor, and the aggregation-induced red shift of their absorption provides selective exploitation of the external light. The temperature increase observed for the SAN, SAN&D, and SANDC treatments should be sufficient for tumor ablation.[15,42] Dox typically exhibits a threshold temperature of 42–43 °C for thermally enhanced cytotoxicity.[43] Conventional hyperthermic strategies require the temperature to be limited to less than 44 °C to avoid systemic side effects.[44] SAN-based photothermal therapy can provide heat to the tumor in a highly selective fashion. As a result, a higher local temperature can be applied, which can increase the synergistic interaction with reduced concerns over the side effects.

The therapeutic efficacy of SANDCs was further studied at the whole-body level. Mice were intravenously administered with SANDC-40, SAN&D-40, SAN, MAN, MAN&D-40, Dox, or saline at 3 day intervals for a total of four treatments (at days 1, 4, 7 and 10). At 24 h after each injection, the mice were exposed to laser irradiation for 5 min (660 nm, 0.5 W/cm^2). To quantitatively evaluate the therapeutic efficacy, changes in the relative tumor volume were recorded for 15 days (Figure 6b). The SANDC, SAN&D, and SAN treatments showed significant suppression of tumor growth. SANDCs showed the largest suppression, exhibiting a complete halt in tumor growth until the last laser irradiation (day 10) and reducing the final tumor size 2 times smaller than that of SAN or SAN&D treatment (see Supporting Information Figure S10 for the magnified portion of Figure 6b). The tumor size was more than 20 times smaller for the SANDC case than the MAN or saline case. MAN&D and Dox showed only slight suppression of tumor growth compared to the MAN and saline cases. The Dox dosage (~2.4 mg kg^{-1})

TABLE 1. Primer Sequences Analyzed for the Quantification of β-Actin, p21, and p32 Protein Expression Levels

	primer sequences
β-actin	sense 5′-TGA GAC CTT CAA CAC CCC AGC-3′
	antisense 5′-GAT GTC ACG CAC GAT TTC CCT-3′
p21	sense 5′-TCT TCT GCT GTG GGT CAG GAG-3′
	antisense 5′-GAG GGC TAA GGC CGA AGA TG-3′
p32	sense 5′-ACA GGG GCA GAA GGC TGA AGA-3′
	antisense 5′-GGT CCG CAA GGA AAT CCA TTA-3′

was not sufficiently high to show significant therapeutic efficacy alone. On the last day, the tumor mass was collected and weighed. The SANDC treatment showed the lightest tumor, followed by SAN, SAN&D, Dox, MAN&D, and MAN, in increasing order of weight (Figure 6c). This result correlates well with the tumor volume change. When the experiment was repeated without laser irradiation, no significant difference was observed in the tumor volume and the final tumor weight among the SANDC, SAN, Dox, MAN&D, MAN, and saline cases (Figure 6d,e). To understand the pathological mechanism of the SANDCs, gene expression levels were studied using quantitative real-time PCR (qRT-PCR). The expression levels of mRNA for pro-apoptotic p32 and p21 proteins were measured from the tumor tissues (Figure 6f). Upregulated p32 and p21 are known results of thermal stress and Dox-induced growth arrest, respectively.[16,45] Only the SAN, SAN&D, and SANDC treatments showed significant p32 levels, which indicate a high thermal stress level caused by the photothermal effect. Remarkably, an elevated expression level of p21 was only observed for SANDCs. Dox at the low dosage was therapeutically effective only when synergistically administered in the SANDC and not for the case of SAN&D or Dox alone. The experiment was repeated without laser irradiation, and no noticeable changes of p32 and p21 were observed (Figure 6g). A TUNEL assay was performed to measure the apoptosis level in tumor tissues after an experiment identical to that for Figure 6b,c. DAPI staining was concurrently performed to identify healthy cells (Figure 6h). The SANDC sample showed the highest TUNEL-positive to DAPI-positive ratio (Figure 6i). The ratio was also high for the SAN&D and SAN samples, which reached approximately 74 and 80% of the value determined for the SANDC, respectively. All other cases (MAN, MAN&D, Dox, and saline) returned a ratio that was less than half of that observed for SANDC. Apoptotic cells were most frequently found for SANDCs, which indicates significant apoptosis-induced cell death and effective tumor regression. Other vital organs, including the liver, spleen, and kidney, were also harvested for their toxicological investigations using H&E staining at day 15 after the administration of SANDC, SAN, SAN&D, Dox, MAN&D, MAN, and saline as for the experiment for Figure 6b,c. For all of the investigated organs irrespective of the administered samples, no noticeable cytotoxic damage was found (Supporting Information Figure S11).

CONCLUSIONS

We report that SANDCs, an engineerable combination cancer therapy platform, can exploit the spatiotemporal concertion between chemo and thermo agents in a controllable and sophisticated manner. SANDCs show a high level of accumulation in tumors without an active tumor-targeting moiety, and they are "doubly" selective as a result of their pH-responsive Dox release and their aggregation-induced absorption shift. This double selectivity has yielded a highly synergistic effect, showing nearly an order of magnitude enhanced cytotoxicity *in vitro* when compared with two sequential independent treatments. This combined therapy significantly reduced the therapeutically effective dosage to a level at which each independent therapy would not show significant efficacy. Using an *in vivo* model, significant tumor growth suppression was demonstrated for the SANDC treatment without noticeable damage to the other organs. SANDC combination therapy demonstrates a means of achieving spatiotemporal concertion at the subcellular, cellular, and organ levels by nanostructure engineering. This concertion of treatment methods led to a highly synergistic effect and to the expansion of the therapeutic window for anticancer reagents, which could minimize side effects.

METHODS

Synthesis of SANDC. A pH-senstive surface molecule that contains a hydrolysis-susceptible citraconic amide moiety was synthesized and introduced to the surface of 10 nm sized citrate gold nanoparticles to obtain SANs as described in the previous report.[9] The following is a typical protocol for SANDC-20 preparation. For other SANDCs, the Dox conjugation ratio was controlled by adjusting the amount of Dox used. Briefly, SANs were purified by centrifugation (using an Amicon ultra 100 kDa MWCO centrifugal filter) and dispersed in 10 mM pH 7.0 phosphate buffer solution to obtain a 500 nM SAN solution. To the SAN solution were added 1 μmol of *N*-(3-dimethylaminopropyl)-*N*′-ethylcarbodiimide hydrochloride (Sigma) and 2 μmol of *N*-hydroxysulfosuccinimide sodium salt (Fluka), and the solution was mixed vigorously at room temperature for 25 min. The activated SANs were purified by repeated centrifugation and dilution with the buffer; this process was repeated three times. Two nanomoles of doxorubicin hydrochloride (Sigma) was dissolved in 50 μL of 50 mM pH 8.0 phosphate buffer solution and mixed with the activated SAN solution. The pH of the solution was 7.4 after mixing. The mixture solution was incubated at room temperature for 3 h. Dox conjugation yield was close to unity; we were not able to find any noticeable free Dox from quantitative analyses such as dialysis and size exclusion chromatography. UV−vis absorption spectra were obtained using an Agilent 8453 UV−vis spectrophotometer, and

fluorescence spectra were measured on a SPEX FluoroLog 3 (Jobin Yvon Horiba) spectrofluorometer.

Fluorescence and Dark-Field Microscopy. B16 F10 mouse melanoma cells were purchased from the Korean Cell Line Bank. B16 F10 cells were maintained in minimum essential medium with Earle's balanced salts (MEM/EBSS, HyClone), which was supplemented with 10% fetal bovine serum (FBS, GIBCO) and 1% penicillin–streptomycin (PS, GIBCO). B16 F10 cells were grown onto 12 mm glass coverslips in 24-well plates at a density of 1×10^5 cells/well at 37 °C under 5% CO_2. After 1 day, the cells were treated with 20 nM SANDC-20. As controls, 20 nM of SAN&D-20, SAN, or 400 nM Dox were used. These samples were incubated for 1, 6, 12, 24, and 48 h at 37 °C under 5% CO_2. The cells were rinsed with PBS three times and fixed with 4% formaldehyde at room temperature for 20 min. The cells were further washed with PBS three times. For counterstaining of the nuclei with 4′,6-diamidino-2-phenylindole (DAPI, Invitrogen), 100 nM DAPI PBS solution was added to the cells and incubated for 5 min. They were then mounted onto slide glasses using an aqueous mounting medium with an antifading agent (Biomeda). The fluorescence and dark-field images were recorded using a Zeiss Axioplan 2 microscope. A high numerical dark-field condenser (0.75–1.0) and a 100×/1.3 oil iris objective (Zeiss) were used for dark-field images. The pictures were taken using a Zeiss Axiocam HR camera.

Relative Viability Levels in Dark Conditions. B16 F10 cell suspension (5000 cells/well) was dispensed in a 96-well plate (Corning) and incubated for 1 day at 37 °C under 5% CO_2. Cells were co-incubated in dark conditions with 20 nM of SANDC-20, SAN&D-20, SAN, or 400 nM Dox. Similarly, cells were co-incubated with 20 nM of SANDC-1 and Dox. These samples were incubated for 1, 3, 6, 9, 12, 24, 36, and 48 h at 37 °C under 5% CO_2. At the end of each incubation time, Cell Counting Kit-8 solution (CCK-8, Dojindo Laboratories) was added to the samples according to the manufacturer's instructions. After further incubation for 2 h, the absorbance at 450 nm was measured using a microplate reader. The results of this measurement were expressed as the ratio between the absorbance of the sample and that of the negative control cells.

Nuclei Isolation and Quantification of Gold Concentration Using ICP-AES. B16 F10 cells (6×10^6) were grown on a 100 mm dish (Corning) and co-incubated for 24 h with 20 nM SAN, SANDC-20, or SAN&D-20. The cells were rinsed with PBS three times, and nuclei were isolated using a nuclei isolation kit (Nuclei EZ Prep Kit, Sigma) according to the manufacturer's instructions. The purity of isolated nuclei was determined by visual microscopic inspection of the nuclei stained by trypan blue, and the nuclei isolation yields were higher than 90% for all of the samples. The nuclei were lysed with aqua regia, and the determination of the gold concentration was performed quantitatively by inductively coupled plasma atomic emission spectrometry (ICP-AES, Thermo Electron Co.).

Investigation of Cellular Distributions of Au NPs Using TEM. B16 F10 cells (1×10^7) were grown on a 100 mm dish and co-incubated for 24 h with 20 nM SANDC-20, SAN&D-20, or SAN. The cells were then fixed with 2.5% glutaraldehyde in a 0.1 M cacodylate buffer (pH 7.2) for 24 h at 4 °C and rinsed three times with cold 0.1 M cacodylate buffer. The cells were fixed with 1% osmium tetraoxide (Ted Pella) for 1 h at 4 °C and washed three times with cold distilled water. They were dehydrated through a series of graded ethanol (50, 60, 70, 80, 90, 95, 98, and 100%) and propylene oxide rinses and finally embedded in epoxy resin (Epon 812). The samples were then polymerized at 60 °C for 24 h, cut into thin slices using an ultramicrotome (Leica), and collected on 200-mesh copper grids. The thin sections of cells were stained with uranyl acetate (2% in ethanol) for 10 min and then with lead citrate for 5 min. They were observed by a Philips Tecnai G2 F20 at 200 kV.

Cancer Therapy at the Cellular Level. B16 F10 cell suspension (5000 cells/well) was dispensed into a 384-well plate (Nunc) and incubated at 37 °C under 5% CO_2 for 1 day. For the SANDC-1 and control cases, 20 nM SANDC-1, Dox, SAN, or SAN&D-1 was co-incubated with cells for 9 h. The cells were then irradiated with a 660 nm cw laser for 1 min at a power density of 8 W/cm^2. To demonstrate the synergistic effect, 20, 200, 400, and 800 nM Dox, 20 nM SAN, SANDCs, or SAN&Ds were co-incubated with cells for 9 h. The cells were irradiated by a 660 nm cw laser for 0, 1, 3, 5, and 10 min at a power density of 8 W/cm^2. Viability was evaluated by adding CCK-8 to each cell solution according to the manufacturer's instructions. After 2 h incubation, the absorbance at 450 nm was measured using a microplate reader. These results were expressed as the ratio of the absorbance of the sample to that of the negative control, which consisted of cells exposed to laser irradiation without sample co-incubation. To determine the threshold power densities, cells (3×10^5 cells/well) were grown onto 12-well plates. After 1 day, the cells were co-incubated with 20 nM SAN, SANDC-40, SAN&D-40, MANDC-40, or 800 nM Dox for 24 h. As a control, cells were incubated without any samples. The cells were rinsed with culture medium three times and exposed to laser irradiation for 5 min at different power densities. Trypan blue was applied to the samples at room temperature for 5 min to reveal cell mortality as blue staining.

Biodistribution of Au NPs in Tumor-Bearing Mice. Four week old female hairless athymic nu/nu mice (20–25 g body weight) were purchased from Orient Bio (Seoul, Korea). The mice were anesthetized with xylazine (10 mg/kg) and ketamine (100 mg/kg), and then B16 F10 cells (1×10^7 cells/mL) were injected subcutaneously into the flank of each mouse. The mice were randomly sorted for treatments when the tumors reached a diameter of 1 cm. They were anesthetized, and 100 μL PBS solutions of SAN, SANDC-40, or MAN were administered intravenously *via* tail vein ($n = 3$). The concentrations were matched for 1 μM Au NPs for SAN and MAN, and 1 μM Au NP and 40 μM Dox for SANDC. They were allowed to circulate for 1, 4, 24, 48, or 72 h. Stomach, heart, lung, spleen, liver, kidney, and tumor tissues were excised after the mice were sacrificed at each time point, followed by lysis using aqua regia. The average weights of tumors for the mice injected with SAN, SANDC, and MAN were 0.47(±0.19), 0.61(±0.28), and 0.64(±0.42) g, respectively. The determination of the gold concentration in each organ and tumor tissue was performed quantitatively by ICP-AES.

Investigation of Tumor Accumulation of Au NPs Using TEM. To determine the intratumoral localization, 1 μM SAN PBS solutions (100 μL) were intravenously injected into the tumor-bearing mice when each tumor reached the size of 1 cm in diameter. The mice were sacrificed at 24 h post-injection, and the tumors were subsequently excised and fixed using 4% formaldehyde solution. The tumors were then fixed with 1% osmium tetraoxide, dehydrated using a series of graded ethanol and propylene oxide, embedded with epoxy resin, and cut into thin slices after polymerization, similar to the method used for the cellular preparations. They were observed by a JEOL JEM-1011 at 100 kV.

Quantification of Gold Accumulation in Tumor Tissues Using Silver Enhancement Staining and CT Analysis. A PBS solution (100 μL) of SAN, SANDC-40, SAN&D-40, MAN, MAN&D-40, Dox, or saline (100 μL) was injected either intravenously or intratumorally into tumor-bearing mice. The concentrations were matched for 5 μM Au NP and 200 μM Dox when they were contained in the sample. For silver enhancement staining, the mice were sacrificed and the tumors were excised after 24 h intravenous injections of samples. Then, tumor tissues were fixed in 10% formalin for 24 h and embedded in paraffin blocks. The blocks were sectioned transversely at a thickness of 4 μm and stained using silver enhancer solution (Sigma) according to the manufacturer's instructions. The silver staining of the tissue sections was examined using a Zeiss Axioplan 2 microscope, and pictures were taken using a Zeiss Axiocam HR camera. For CT analysis, the tumor tissues were fixed in a 10% phosphate-buffered formaldehyde solution for 24 h at 1 day post- intravenous injections or 1, 2, 3 day post-intratumoral injections. The CT images of tumor tissues were obtained with a micro-CT system (SkyScan-1076; Skyscan, 40 kV, 250 mA). CT images were also obtained from living mice on day 3 after intravenous injections of samples. CT image processing and Hounsfield unit calculation were performed using CT analyzer software (Skyscan).

Cancer Therapy at the Whole-Body Level. Four week old female hairless athymic nu/nu mice (20–25 g body weight) were

anesthetized, and B16 F10 cells (1×10^6) were injected subcutaneously into the flank of each mouse. The mice were randomly sorted for treatments when the tumors reached approximately 5−10 mm in diameter as measured with a digital caliper (within 2 weeks of subcutaneous injection of B16 F10 cells). The mice were anesthetized, and a 100 μL PBS solution of SANDC-40 (n = 9), SAN (n = 8), SAN&D-40 (n = 8), Dox (n = 9), MAN&D-40 (n = 8), MAN (n = 8), or saline (n = 6) was intravenously injected *via* the tail vein. The concentrations were matched for 5 μM Au NPs and 200 μM Dox when they were contained in the sample. The mice were periodically injected with each sample at 3 day intervals for a total of four treatments (days 1, 4, 7, and 10). The samples were allowed to circulate for 24 h to accumulate in the tumors prior to laser exposure. After 24 h post-injection, the tumors were either exposed to laser light (660 nm cw diode laser, *ca.* 1 cm diameter, 0.5 W/cm^2) for 5 min under anesthesia or to anesthesia without irradiation. The sizes of the tumors were measured at regular intervals using a digital caliper, and the tumor volume was estimated by ellipsoidal calculation as $V = (\text{width})^2 \times \text{length} \times \pi/6$. Errors are reported as the standard deviation of the mean, and the significance was determined using the unpaired, two-tailed *t*-test. The animal study was approved by the Institutional Animal Care and Use Committee of Seoul National University (No. SNU-100422-5).

qRT-PCR Result of p21 and p32 Protein Expression Levels of Tumor Tissues. Tumors harvested at day 15 were homogenized and lysed in TRIzol reagent (Invitrogen). Total RNA was extracted with chloroform and precipitated with 80% (v/v) isopropyl alcohol. After the supernatant was removed, the RNA pellet was washed with 75% ethanol, air-dried, and dissolved in 0.1% diethyl pyrocarbonate-treated water. The RNA concentration was determined by measuring the absorbance at 260 nm using a UV−vis spectrophotometer. Reverse transcription was performed using 5 μg of pure total RNA and SuperScriptTM II reverse transcriptase (Invitrogen). The qRT-PCR reactions were performed for β-actin, p21, and p32 mRNA using a Light Cycler 480 (Roche) with SYBR Green I (TAKARA). After preincubation for 5 min, 35 amplification cycles were performed. Each cycle consisted of the following three steps: 30 s at 94 °C, 45 s at 60 °C, and 45 s at 72 °C. The primer sequences for qRT-PCR are shown in Table 1. All data were analyzed using the $2^{-\Delta\Delta C_t}$ method.

Toxicological Investigations Using the TUNEL Assay. Mice were sacrificed at day 15, and tumors were harvested for use in toxicological investigations. The tumor tissues were fixed in 10% formalin for 24 h and embedded in paraffin blocks. The blocks were sectioned transversely at a thickness of 4 μm. The TUNEL assay was performed to determine the apoptotic activity of the tumor tissues using an ApopTag Red *in situ* apoptosis detection kit (Millipore) according to the manufacturer's instructions.

Conflict of Interest: The authors declare no competing financial interest.

Acknowledgment. This work was supported by the KOSEF grant funded by MOST 20120006280, the Korea Health 21 R&D Project Ministry of Health & Welfare (A121763), the Priority Research Center Program through NRF 2009-0094036, NRF funded by the Ministry of Education, Science and Technology (2010-0020352, 20120005973), Nuclear R&D (grant code: 20090081817) program of NRF, and the grant (A100443) from the Korean Health 21 R&D project, Ministry of Health and Welfare, Republic of Korea.

Supporting Information Available: Experimental details and supporting figures. This material is available free of charge *via* the Internet at http://pubs.acs.org.

REFERENCES AND NOTES

1. Hahn, G. M.; Braun, J.; Har-Kedar, I. Thermochemotherapy: Synergism between Hyperthermia (42−43 Degrees) and Adriamycin (of Bleomycin) in Mammalian Cell Inactivation. *Proc. Natl. Acad. Sci. U.S.A.* **1975**, *72*, 937–940.
2. Dahl, O. Chemopotentiation by Hyperthermia. In *Chemopotentiation by Hyperthermia*; Urano, M., Douple, E., Eds.; VSP BV: Utrecht, The Netherlands, 1994; Vol. 4, pp 9−28.
3. Dahl, O. Thermoradiotherapy and Thermochemotherapy. In *Thermoradiotherapy and Thermochemotherapy*; Seegenschmiedt, M. H., Fessenden, P., Vernon, C. C., Eds.; Springer: Berlin, 1995; Vol. 1, pp 103−121.
4. Urano, M. Invited Review: For the Clinical Application of Thermochemotherapy Given at Mild Temperatures. *Int. J. Hyperthermia* **1999**, *15*, 79–107.
5. Hirsch, L. R.; Stafford, R. J.; Bankson, J. A.; Sershen, S. R.; Rivera, B.; Price, R. E.; Hazle, J. D.; Halas, N. J.; West, J. L. Nanoshell-Mediated Near-Infrared Thermal Therapy of Tumors under Magnetic Resonance Guidance. *Proc. Natl. Acad. Sci. U.S.A.* **2003**, *100*, 13549–13554.
6. Lal, S.; Clare, S. E.; Halas, N. J. Nanoshell-Enabled Photothermal Cancer Therapy: Impending Clinical Impact. *Acc. Chem. Res.* **2008**, *41*, 1842–1851.
7. Huang, X.; Neretina, S.; El-Sayed, M. A. Gold Nanorods: From Synthesis and Properties to Biological and Biomedical Applications. *Adv. Mater.* **2009**, *21*, 4880–4910.
8. von Maltzahn, G.; Park, J.-H.; Agrawal, A.; Bandaru, N. K.; Das, S. K.; Sailor, M. J.; Bhatia, S. N. Computationally Guided Photothermal Tumor Therapy Using Long-Circulating Gold Nanorod Antennas. *Cancer Res.* **2009**, *69*, 3892–3900.
9. Nam, J.; Won, N.; Jin, H.; Chung, H.; Kim, S. pH-Induced Aggregation of Gold Nanoparticles for Photothermal Cancer Therapy. *J. Am. Chem. Soc.* **2009**, *131*, 13639–13645.
10. Cobley, C. M.; Au, L.; Chen, J.; Xia, Y. Targeting Gold Nanocages to Cancer Cells for Photothermal Destruction and Drug Delivery. *Expert Opin. Drug Delivery* **2010**, *7*, 577–587.
11. von Maltzahn, G.; Park, J.-H.; Lin, K. Y.; Singh, N.; Schwöppe, C.; Mesters, R.; Berdel, W. E.; Ruoslahti, E.; Sailor, M. J.; Bhatia, S. N. Nanoparticles That Communicate *in Vivo* To Amplify Tumour Targeting. *Nat. Mater.* **2011**, *10*, 545–552.
12. Hauck, T. S.; Jennings, T. L.; Yatsenko, T.; Kumaradas, J. C.; Chan, W. C. W. Enhancing the Toxicity of Cancer Chemotherapeutics with Gold Nanorod Hyperthermia. *Adv. Mater.* **2008**, *20*, 3832–3838.
13. Park, H.; Yang, J.; Lee, J.; Haam, S.; Choi, I.-H.; Yoo, K.-H. Multifunctional Nanoparticles for Combined Doxorubicin and Photothermal Treatments. *ACS Nano* **2009**, *3*, 2919–2926.
14. You, J.; Zhang, G.; Li, C. Exceptionally High Payload of Doxorubicin in Hollow Gold Nanospheres for Near-Infrared Light-Triggered Drug Release. *ACS Nano* **2010**, *4*, 1033–1041.
15. Lee, S. M.; Park, H.; Yoo, K. H. Synergistic Cancer Therapeutic Effects of Locally Delivered Drug and Heat Using Multifunctional Nanoparticles. *Adv. Mater.* **2010**, *22*, 4049–4053.
16. Park, J.-H.; von Maltzahn, G.; Xu, M. J.; Fogal, V.; Kotamraju, V. R.; Ruoslahti, E.; Bhatia, S. N.; Sailor, M. J. Cooperative Nanomaterial System to Sensitize, Target, and Treat Tumors. *Proc. Natl. Acad. Sci. U.S.A.* **2010**, *107*, 981–986.
17. Lee, S.-M.; Park, H.; Choi, J.-W.; Park, Y. N.; Yun, C.-O.; Yoo, K.-H. Multifunctional Nanoparticles for Targeted Chemophotothermal Treatment of Cancer Cells. *Angew. Chem., Int. Ed.* **2011**, *50*, 7581–7586.
18. Chithrani, B. D.; Ghazani, A. A.; Chan, W. C. W. Determining the Size and Shape Dependence of Gold Nanoparticle Uptake into Mammalian Cells. *Nano Lett.* **2006**, *6*, 662–668.
19. Choi, H. S.; Liu, W.; Misra, P.; Tanaka, E.; Zimmer, J. P.; Itty Ipe, B.; Bawendi, M. G.; Frangioni, J. V. Renal Clearance of Quantum Dots. *Nat. Biotechnol.* **2007**, *25*, 1165–1170.
20. Goode, J. A.; Chadwick, D. J. *The Tumour Microenvironment: Causes and Consequences of Hypoxia and Acidity*; John Wiley & Sons, Ltd: New York, 2001.
21. Ulbrich, K.; Subr, V. Polymeric Anticancer Drugs with pH-Controlled Activation. *Adv. Drug Delivery Rev.* **2004**, *56*, 1023–1050.
22. Minotti, G.; Menna, P.; Salvatorelli, E.; Cairo, G.; Gianni, L. Anthracyclines: Molecular Advances and Pharmacologic Developments in Antitumor Activity and Cardiotoxicity. *Pharmacol. Rev.* **2004**, *56*, 185–229.

23. Brinegar, A. C.; Kinsella, J. E. Reversible Modification of Lysine in Soybean Proteins, Using Citraconic Anhydride: Characterization of Physical and Chemical Changes in Soy Protein Isolate, the 7s Globulin, and Lipoxygenase. *J. Agric. Food Chem.* **1980**, *28*, 818–824.
24. Lee, Y.; Fukushima, S.; Bae, Y.; Hiki, S.; Ishii, T.; Kataoka, K. A Protein Nanocarrier from Charge-Conversion Polymer in Response to Endosomal pH. *J. Am. Chem. Soc.* **2007**, *129*, 5362–5363.
25. Mok, H.; Park, J. W.; Park, T. G. Enhanced Intracellular Delivery of Quantum Dot and Adenovirus Nanoparticles Triggered by Acidic pH *via* Surface Charge Reversal. *Bioconjugate Chem.* **2008**, *19*, 797–801.
26. Verma, A.; Uzun, O.; Hu, Y.; Hu, Y.; Han, H.-S.; Watson, N.; Chen, S.; Irvine, D. J.; Stellacci, F. Surface-Structure-Regulated Cell-Membrane Penetration by Monolayer-Protected Nanoparticles. *Nat. Mater.* **2008**, *7*, 588–595.
27. Park, J.; Nam, J.; Won, N.; Jin, H.; Jung, S.; Jung, S.; Cho, S.-H.; Kim, S. Compact and Stable Quantum Dots with Positive, Negative, or Zwitterionic Surface: Specific Cell Interactions and Non-specific Adsorptions by the Surface Charges. *Adv. Funct. Mater.* **2011**, *21*, 1558–1566.
28. González, R. C.; Woods, R. E.; Eddins, S. L. *Digital Image Processing Using Matlab*; Prentice Hall: New York, 2004.
29. Won, N.; Jeong, S.; Kim, K.; Kwag, J.; Park, J.; Kim, S. G.; Kim, S. Imaging Depths of Near-Infrared Quantum Dots in First and Second Optical Windows. *Mol. Imaging* **2012**, *11*, 1536-0121.
30. Kang, B.; Mackey, M. A.; El-Sayed, M. A. Nuclear Targeting of Gold Nanoparticles in Cancer Cells Induces DNA Damage, Causing Cytokinesis Arrest and Apoptosis. *J. Am. Chem. Soc.* **2010**, *132*, 1517–1519.
31. Kiyomiya, K.-i.; Matsuo, S.; Kurebe, M. Mechanism of Specific Nuclear Transport of Adriamycin. *Cancer Res.* **2001**, *61*, 2467–2471.
32. Pante, N.; Kann, M. Nuclear Pore Complex Is Able To Transport Macromolecules with Diameters of ~39 nm. *Mol. Biol. Cell* **2002**, *13*, 425–434.
33. Pan, L.; He, Q.; Liu, J.; Chen, Y.; Ma, M.; Zhang, L.; Shi, J. Nuclear-Targeted Drug Delivery of Tat Peptide-Conjugated Monodisperse Mesoporous Silica Nanoparticles. *J. Am. Chem. Soc.* **2012**, *134*, 5722–5725.
34. Eliyahu, H.; Barenholz, Y.; Domb, A. Polymers for DNA Delivery. *Molecules* **2005**, *10*, 34–64.
35. Balogh, L.; Nigavekar, S. S.; Nair, B. M.; Lesniak, W.; Zhang, C.; Sung, L. Y.; Kariapper, M. S. T.; El-Jawahri, A.; Llanes, M.; Bolton, B.; *et al.* Significant Effect of Size on the *In Vivo* Biodistribution of Gold Composite Nanodevices in Mouse Tumor Models. *Nanomed. Nanotechnol. Biol. Med.* **2007**, *3*, 281–296.
36. Hirn, S.; Semmler-Behnke, M.; Schleh, C.; Wenk, A.; Lipka, J.; Schäffler, M.; Takenaka, S.; Möller, W.; Schmid, G.; Simon, U.; *et al.* Particle Size-Dependent and Surface Charge-Dependent Biodistribution of Gold Nanoparticles after Intravenous Administration. *Eur. J. Pharm. Biopharm.* **2011**, *77*, 407–416.
37. Choi, W. I.; Kim, J.-Y.; Kang, C.; Byeon, C. C.; Kim, Y. H.; Tae, G. Tumor Regression *in Vivo* by Photothermal Therapy Based on Gold-Nanorod-Loaded, Functional Nanocarriers. *ACS Nano* **2011**, *5*, 1995–2003.
38. You, J.; Zhang, R.; Zhang, G.; Zhong, M.; Liu, Y.; Van Pelt, C. S.; Liang, D.; Wei, W.; Sood, A. K.; Li, C. Photothermal-Chemotherapy with Doxorubicin-Loaded Hollow Gold Nanospheres: A Platform for Near-Infrared Light-Trigged Drug Release. *J. Controlled Release* **2012**, *158*, 319–328.
39. Kim, B.; Han, G.; Toley, B. J.; Kim, C.-k.; Rotello, V. M.; Forbes, N. S. Tuning Payload Delivery in Tumour Cylindroids Using Gold Nanoparticles. *Nat. Nanotechnol.* **2010**, *5*, 465–472.
40. Perrault, S. D.; Walkey, C.; Jennings, T.; Fischer, H. C.; Chan, W. C. W. Mediating Tumor Targeting Efficiency of Nanoparticles through Design. *Nano Lett.* **2009**, *9*, 1909–1915.
41. Popović, Z.; Liu, W.; Chauhan, V. P.; Lee, J.; Wong, C.; Greytak, A. B.; Insin, N.; Nocera, D. G.; Fukumura, D.; Jain, R. K.; *et al.* A Nanoparticle Size Series for *In Vivo* Fluorescence Imaging. *Angew. Chem., Int. Ed.* **2010**, *49*, 8649–8652.
42. Dickerson, E. B.; Dreaden, E. C.; Huang, X.; El-Sayed, I. H.; Chu, H.; Pushpanketh, S.; McDonald, J. F.; El-Sayed, M. A. Gold Nanorod Assisted Near-Infrared Plasmonic Photothermal Therapy (PPTT) of Squamous Cell Carcinoma in Mice. *Cancer Lett.* **2008**, *269*, 57–66.
43. Bull, J. M. C. An Update on the Anticancer Effects of a Combination of Chemotherapy and Hyperthermia. *Cancer Res.* **1984**, *44*, 4853s–4856s.
44. van der Zee, J. Heating the Patient: A Promising Approach? *Ann. Oncol.* **2002**, *13*, 1173–1184.
45. Chang, B.-D.; Swift, M. E.; Shen, M.; Fang, J.; Broude, E. V.; Roninson, I. B. Molecular Determinants of Terminal Growth Arrest Induced in Tumor Cells by a Chemotherapeutic Agent. *Proc. Natl. Acad. Sci. U.S.A.* **2002**, *99*, 389–394.